Letter to the Editor

Whole body positron emission tomography-MRI of Erdheim-Chester disease: a case report

Nunzia Garbino[1#], Bruna Punzo[1#], Antonio Todisco[2], Giovanni Cirillo[2], Carlo Cavaliere[1]

[1]IRCCS SDN, Naples, Italy; [2]Division of Human Anatomy, Neuronal Networks Morphology Lab, Department of Mental, Physical Health and Preventive Medicine, University of Campania "Luigi Vanvitelli", Naples, Italy

[#]These authors contributed equally to this work.

Correspondence to: Dr. Carlo Cavaliere, MD. IRCCS SDN, Via E. Gianturco 113, 80142, Naples, Italy. Email: ccavaliere@sdn-napoli.it.

Submitted Nov 14, 2019. Accepted for publication Jul 10, 2020.
doi: 10.21037/qims-19-953
View this article at: http://dx.doi.org/10.21037/qims-19-953

Introduction

Erdheim-Chester disease (ECD) is a rare non-Langerhans cells systemic histiocytosis characterized by multiple lesions that can involve several organs and systems [including central nervous system (CNS), bones, skin, heart and vessels] and produce a highly heterogeneous clinical picture (1). Therefore, a correct patient diagnostic work-flow has to be based on a multidisciplinary approach, including the clinical examination, histopathology and integrated imaging (2). Indeed, imaging plays a key role in the diagnosis of ECD, often requiring the combination of bone scintigraphy for skeletal assessment (1), radiography (RX), computed tomography (CT), and magnetic resonance imaging (MRI) for characterization of specific organ involvement (3), and ^{18}F-fluorodeoxyglucose (^{18}F-FDG) positron emission tomography (PET)-CT for systemic evaluation and treatment assessment (4).

To date, combined PET-MRI is the most complex and sophisticated hybrid imaging platform available whole-body imaging assessment. PET-MRI combines molecular information of PET with excellent anatomic details of MRI systems and overcoming limitations of each modality alone (5).

We here describe for the first-time simultaneous PET-MRI findings in a patient affected by ECD, showing multi-systemic involvement in a single shot imaging session.

Materials and methods

PET/CT acquisition was performed on a Gemini TF (Philips Medical Systems, Best, The Netherlands) tomograph designed with a multi-ring LYSO block detectors system, as previously reported (6). PET data was acquired in sinogram mode for 15 min with a matrix size of 144 × 144. PET data were reconstructed using the LOR-TF-RAMLA algorithm; therefore data was post filtered with a three-dimensional isotropic gaussian of 4 mm at FWHM. CT-based attenuation maps were created with a low dose CT scan (120 kV, 80 mA) using commonly employed bi-linear scaling. The acquisition time was 3 min per bed position (BP), with 5\6 BPs (each 21 cm) covering the trunk of the patients starting from the pelvis and moved up toward the head. The result was a total PET/CT acquisition time of approximately 15 min.

Following, about 20 min after the start of the PET/CT acquisition and using the same radiotracer injection, a PET/MR scan was started. Whole-body PET-MRI data were simultaneously acquired using a scanner 3 Tesla Biograph mMR tomograph (Siemens Healthineers, Erlangen, Germany) about 70 minutes after the 380 MBq ^{18}F-FDG administration. PET data were reconstructed with an AW OSEM 3D iterative reconstruction algorithm. MR attenuation correction was performed via a segmentation approach based on 2-point Dixon MRI sequences.

During PET acquisition, MRI was acquired using 32 channels body coil and 12 channels phased array brain coil combined to form a multichannel coil by using total imaging matrix technology. For the whole-body study, we considered the following MRI sequences: T1-weighted and T2-weighted short time inversion recovery (STIR),

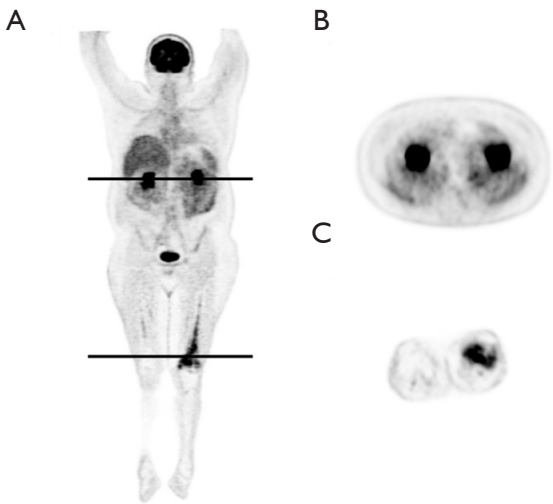

Figure 1 Positron emission tomography (PET) alterations in Erdheim-Chester disease (ECD). (A) Maximum intensity projection (MIP) of whole-body PET showing a modest and inhomogeneous uptake of ^{18}F-fluorodeoxyglucose (^{18}F-FDG) at the level of kidneys and perirenal regions (B) and distal segment of the left femur (C).

acquired in coronal planes; T2-weighted and diffusion weighted imaging (DWI), in axial planes; 3D fat-suppressed T1-weighted gradient-echo (VIBE) sequence, acquired in coronal direction before and after gadolinium-based contrast (Gadovist 1.0 mmol/mL, Bayer) injection. In the same session, dedicated sequences for the heart and brain study were included. The result was a total PET/MR acquisition time of approximately 40 min for the whole-body acquisition.

Dual source computed tomography (DSCT) was performed with a 3rd generation dual source multidetector scanner (Somatom Force, Siemens Healthineers, Erlangen, Germany). At first, a non-contrast scan was detected to evaluate possible presence of calcifications. Tube voltage was adjusted by the use of an automated attenuation-based tube voltage selection functionality (CARE kV, Siemens). Following, 90 mL of iodinated contrast agent (Iomeprol 400 mgI/mL, Iomeron 400, Bracco, Italy) at 2.0 mL/s followed by 30 mL of saline at the same flow were injected. Data were reconstructed by a dedicated 3rd generation advanced modelled iterative reconstruction (ADMIRE, Siemens Healthineers, Erlangen, Germany) using medium sharp convolution kernels (Br40), strength level of 3, section thickness of 1.0.

The study was approved by institutional ethics committee board of IRCCS Pascale (NO.: 3/17) and written informed consent was obtained from the patient for publication of this manuscript and any accompanying images.

Results

A 53-year-old man was diagnosed with neurohistiocytosis and referred to our institution for the imaging work-flow. He was affected by pan-hypopituitarism (diabetes insipidus, hypogonadism and hypocorticosurrenalism) and at neurological examination presented bilateral exophthalmos and a cerebellar syndrome, consisting of ataxic gait, nystagmus and dysarthria.

Previously, two cutaneous translucent papular lesions in pectoral and popliteal region were removed and processed for morphological analysis. The histopathological analysis revealed a widespread infiltration of dermis by CD68$^+$ and CD163$^+$ histiocytes, suggestive of a xantogranuloma, a non-Langerhans cell histiocytic lesion (2).

To narrow the diagnosis among systemic histiocytic disorders of adults, we performed an extensive imaging protocol based on the PET/CT and PET-MRI.

PET imaging showed a modest and inhomogeneous uptake of ^{18}F-FDG at the level of kidneys, perirenal regions [max standardized uptake values (SUV) =2.8] (*Figure 1A,B*) and at the distal segment of the left femur (max SUV = 6.8) (*Figure 1C*).

Whole body MRI demonstrated: a mild inhomogeneity of the bilateral retro-orbitary fat (*Figure 2A*); a mild concentric thickening of the aorta wall in its thoracic tract, showing a discrete enhancement after contrast injection and generally referred as "*coated aorta sign*" (*Figure 2B*); a diffused

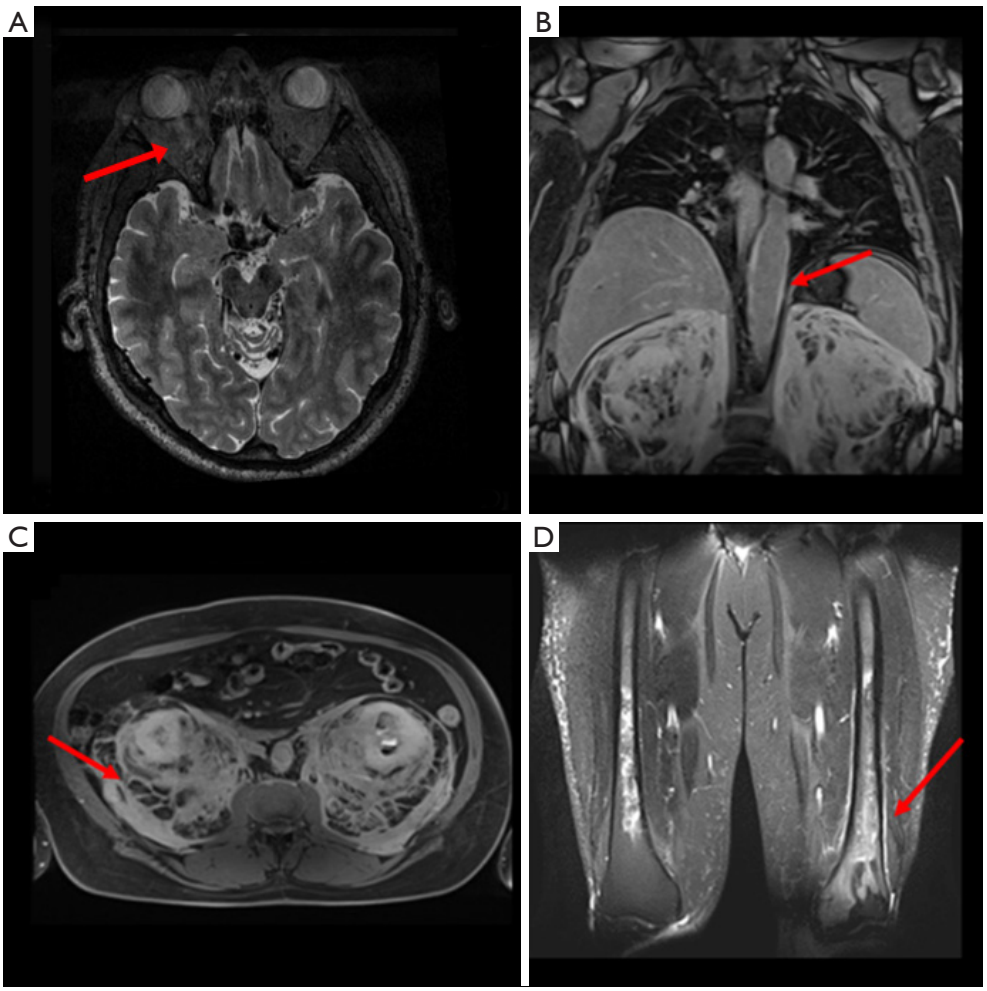

Figure 2 Whole body MRI findings in Erdheim-Chester disease (ECD). (A) Volumetric sequence showing mild inhomogeneity of retro-orbitary fat (red arrow); (B) Coronal T1-weigthed image after e.v. contrast injection showing a longitudinal concentric thickening of the aorta wall, known as *coated aorta sign* (red arrow); (C) Abdominal axial T1 showing diffuse inhomogeneity of the perirenal space, known as hairy kidney sign (red arrow); (D) coronal STIR image showing medullary sclerotic lesions of both the femurs (red arrow).

and inhomogeneous thickening of the retroperitoneal perirenal space of both sides (volume: 8,472.36 cm^3), showing enhancement after contrast injection, and typically referred as "*hairy kidney sign*" (*Figure 2C*); an asymmetric sclerotic alteration of the distal portion of both femurs, more pronounced on the left side (volume: 20 cm^3) (*Figure 2D*).

Brain MRI demonstrated: an empty sella (ES), showing pituitary gland shrinking and cerebrospinal fluid filling the sella turcica (*Figure 3A*); an enlargement of the cerebellar subarachnoid spaces due to mild atrophy of the cerebellar vermis (*Figure 3B*); a mild asymmetric T2/FLAIR hyperintensity nearby the dentate nuclei and in the white matter around the fourth ventricle (*Figure 3C*).

Cardiac MRI highlighted a solid mass with a diameter of 34 mm and a longitudinal length of 50 mm in the right atrio-ventricular sulcus, well visible in the four-chambers view, and compatible with a typical localization of ECD (*Figure 4*).

Based on PET-MRI findings, a DSCT acquisition was performed to detail perirenal and bone alterations. The DSCT investigation confirmed retroperitoneal fibrotic thickening and femoral bone involvement, already detected by PET-MRI and suggested by CT-coregistered PET (*Figure 5A,B*) and allowed a better morphological characterization of the coated aorta alteration (*Figure 5C,D*).

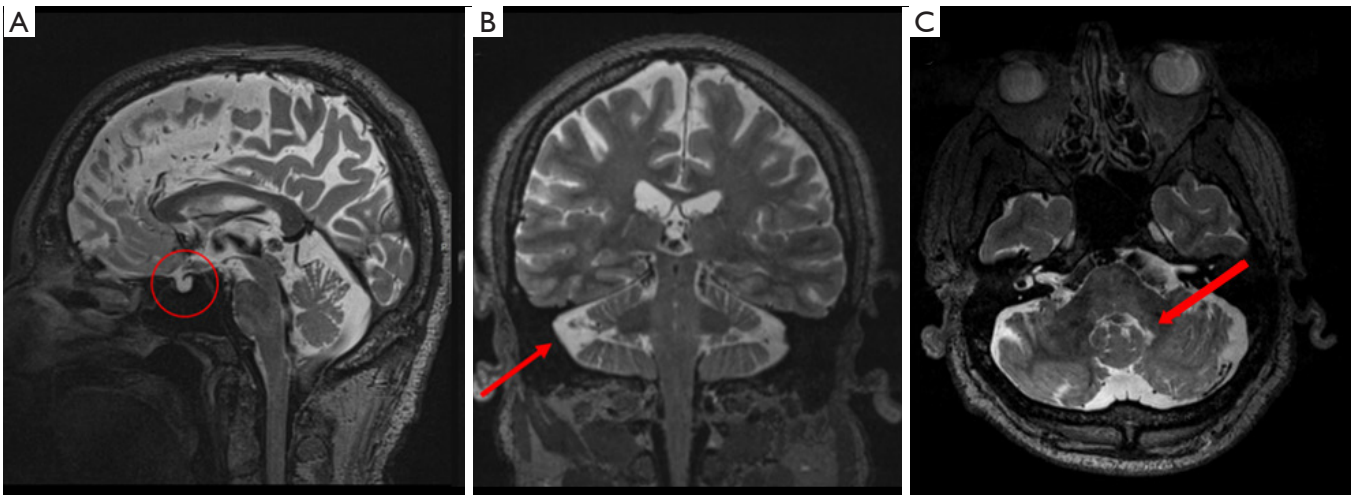

Figure 3 Brain MRI findings in Erdheim-Chester disease (ECD). (A) The red circle shows the empty sella (ES), with the sella occupied by a cerebrospinal fluid diverticulum; (B) Enlargement of cerebellar subarachnoid spaces was highlighted (red arrow); (C) Volumetric sequence T2-weighted showing an hyperintense signal alteration around the 4th ventricle on axial plane, mainly on the left side (red arrow).

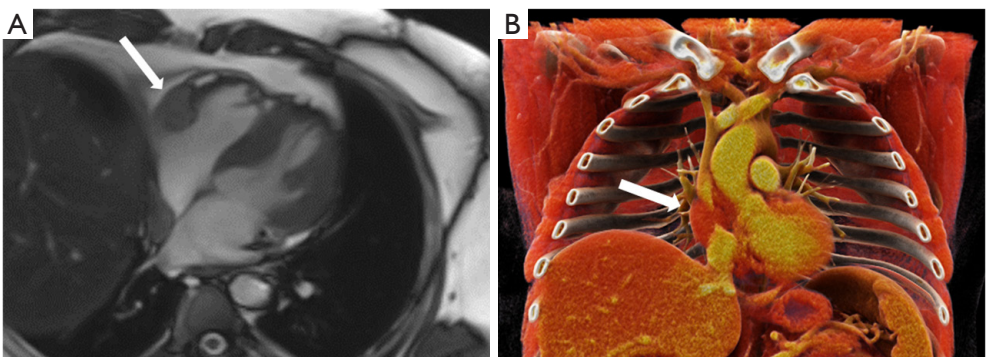

Figure 4 Cardiac involvement in Erdheim-Chester disease (ECD). (A) 4 chamber view of cardiac MRI showing a solid mass in right atrio-ventricular sulcus (white arrow); (B) 3D Cinematic Rendering of dual source computed tomography (DSCT) acquisition (white arrow).

Discussion

ECD is a rare non-Langerhans cells histiocytosis, characterized by systemic infiltration of histiocytes in various organs, causing multiple lesions responsible for a very heterogeneous clinical picture (7). ECD mostly affects male adults between the 5^{th}–7^{th} decades of life. The most common presentation symptom is bone pain, followed by panhypopituitarism and neurological symptoms (ponto-cerebellar dysfunction) (8).The pathogenesis of this heterogeneous histiocytic disorder is still object of debate; however, the identification of the clonal nature of the disorder and the BRAF*V600* mutation, are progressively reformulating our understanding of the pathogenesis and clinical management of the disease (9).

From the first description by William Chester in 1930 (10), almost 550 cases have been reported and the number of cases has dramatically increased in the last 10 years due to increased recognition of the disease.

The diagnosis of ECD depends on the combination of histopathologic findings ($CD68^+$, $CD163^+$, $CD1a^-$ histiocytes) in the appropriate clinical and imaging context (1,11).

The latter plays a key role in diagnosis of ECD. In particular we highlighted the significance of the integration of PET scan combined with MRI, exploiting the ability to provide functional and morphological information that have a significant impact in diagnostic assessment, patient management and potentially outcome.

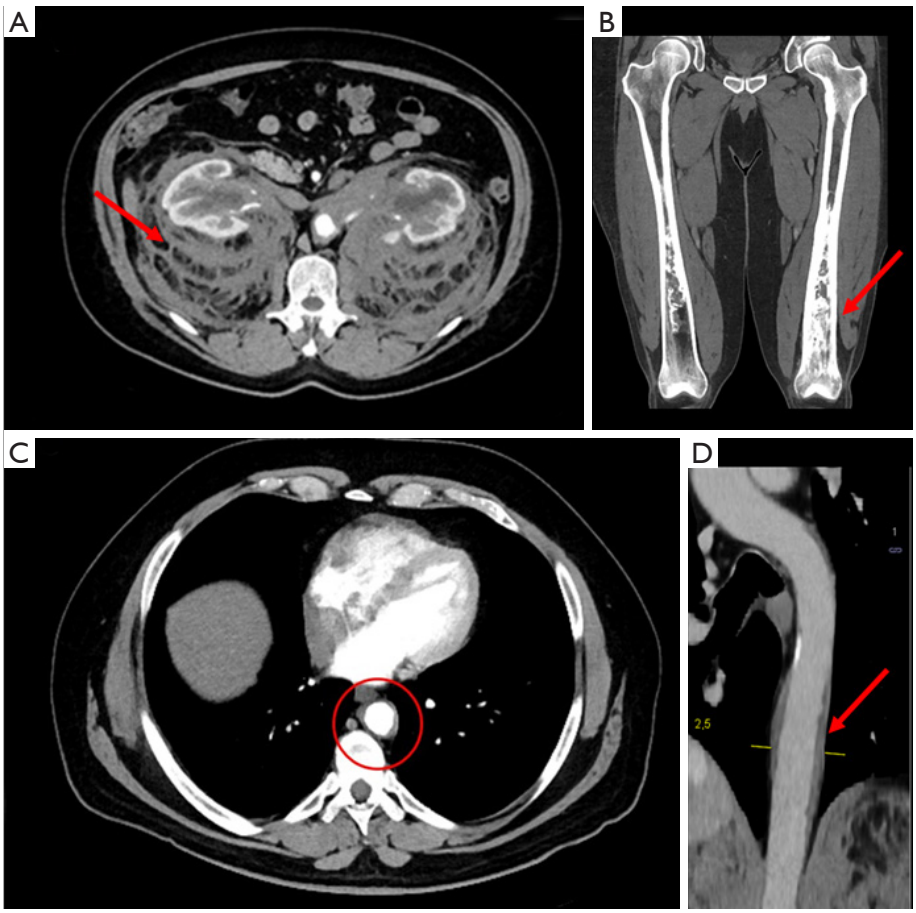

Figure 5 Dual source computed tomography (DSCT) findings in Erdheim-Chester disease (ECD). (A) Axial CT scan showing *hairy kidney sign* (red arrow); (B) Coronal CT multiplanar reconstruction showing an asymmetric sclerotic lesion of both the femurs (red arrow); (C) Axial view of thoracic DSCT displaying the "*coated aorta sign*" (red circle); (D) Curved Multiplanar Reconstruction (c-MPR) of thoracic aorta with wall concentric thickening (red arrow).

Generally ECD is assessed through PET/CT exam, which plays an important role in the management of this disorder and its complications. In fact this method allows to evaluate the extent of the disease by detecting visceral and vascular infiltration, excluding systemic involvement, identifying the site for biopsy and evaluating the response to therapy. Furthermore, it appears to be equally sensitive for the evaluation of bone involvement (12). Although PET/CT is the most common technique used for the evaluation of systemic diseases such as ECD, PET/MRI shows itself as a promising diagnostic imaging technique for the exceptional resolution of contrast of soft tissues and for the intrinsic multiparametric ability of the method that provides additional information to that obtained with the PET scan alone (13). In addition, the risk of developing radiation-induced malignancies can be reduced by lower patient exposure (14). In anatomical areas such as brain, neck and heart, MRI is superior in the evaluation of the typical lesions of the disorder. However, the acquisition times are longer than PET/CT (40 *vs.* 15 min for the whole-body exam), increasing the possibility of movement artifacts, especially in fragile or non-compliant patients. In our study, although the acquisition times are relatively long, we found that the information obtained from PET/MRI is comparable to PET/CT and greater for several regions, such as heart and brain, which are better described and assessable through MRI (15).

ECD disorder can compromise more different anatomical areas such as skeletal involvement that is highly pronounced and it occurs in up to 96% of cases (16). It consists of

symmetric diaphyseal and metaphyseal osteosclerosis of distal limb bones, which is the reason for bone pain, the most frequent patient's symptom in approximately 50% of the patients (17). Here bilateral medullary osteosclerotic lesions in both femurs were detected by MRI scan while PET was able to identify hypermetabolism only in the left side lesion and depicted in fused PET-MR images. Furthermore, MRI was considered the method to study the extent of medullary involvement and to rule out associated osteonecrosis, which may occur primarily due to the disease or as an adverse effect of chemotherapy, suggesting a role for PET-MRI also for the patient follow-up (18).

The frequency of CNS involvement in ECD varies from 25% to 50%, accounting for functional disability and representing an independent predictor of death (18,19). Infiltrations and lesions can occur throughout the neuraxis, both in the intra-axial and extra-axial compartments and present with focal symptoms, referable to compression or infiltrations of local structures. Intra-axial ECD lesions are commonly observed in the cerebellum or in the pons, causing progressive cerebellar and brainstem dysfunction (20). Conversely, our patient did not show macroscopic lesions in the pons and cerebellum, except for a mild asymmetric hyperintensity in T2 sequence in the white matter around the fourth ventricle, and nearby the dentate nuclei. The infiltration of the pituitary gland is responsible of the endocrinopathy observed in ECD, occurring in almost 25% of patients. The most common disorder is the diabetes insipidus, followed by hyperprolactinemia, gonadotropin insufficiency, and hypotestosteronism. MRI is the gold-standard exam to highlight ESS, enlargement and abnormal enhancement of the pituitary gland, stalk, and hypothalamus (21). Our patient has been complaining of the pituitary disorder for 10 years, thus representing one of the symptoms at the disease onset. In this case, MRI allowed to identify the ES alteration, highlighting the added value of PET-MRI compared to other hybrid techniques to investigate highly complex soft tissue pathologies (22).

Unilateral or bilateral infiltration of the orbits occurs in nearly 15–25% of patients presenting with exophthalmos, retro-orbital pain, or visual disturbances (20). Orbital lesions need to be differentiated from other common conditions such as Graves disease, granulomatous disorders, lymphomas, and giant cell arteritis. Our patient presented bilateral exophthalmos and PET-MRI showed retro-orbitary fat inhomogeneity.

A further advantage offered by the PET-MRI acquisition is the characterization of cardiac and cardiovascular involvement, mostly asymptomatic and present in about 75% of cases (23). Commonly, it is related to a poor chemotherapy response and to death due to other complications (e.g., cardiac conduction defects, or valvular insufficiency). Our patient presents a circumferential infiltration of the thoracic and abdominal aorta which appeared as T1 hyperintense enhancing signal at PET-MRI and as enhancing soft-tissue attenuation at DSCT. Moreover, several studies have reported solid masses located in the paracardiac region (23), also detected here by MRI sequences, which shows not enhancing mass at the right atrio-ventricular sulcus without a significant uptake at the concurrent PET acquisition.

Hydronephrosis, ureteral narrowing and retroperitoneal fibrosis are common consequences of the infiltration of the perirenal tissues, leading to the appearance of the "hairy kidney sign" (24). PET showed a modest and inhomogeneous uptake of ^{18}F-FDG at the perirenal regions, corresponding to fibrosis area detected by MRI.

Concluding, PET-MRI provides a better characterization of the extent and the regional degree of impairment in this multi-organ condition, demonstrating on higher diagnostic accuracy mainly in districts like brain and heart, where the PET alone in missing. Therefore, PET-MRI allows fully investigation of the systemic involvement in ECD, combining in a single imaging session MRI high contrast resolution and ^{18}F-FDG-PET sensitivity.

Acknowledgments

Funding: This work was supported by "Ricerca Corrente" Grant from Italian Ministry of Health (IRCCS SDN).

Footnote

Conflicts of Interest: All authors have completed the ICMJE uniform disclosure form (available at http://dx.doi.org/10.21037/qims-19-953). The authors have no conflicts of interest to declare.

Ethical Statement: The study was approved by institutional ethics committee board of IRCCS Pascale (NO.: 3/17) and written informed consent was obtained from the patient for publication of this manuscript and any accompanying images.

References

1. Young JR, Johnson GB, Murphy RC, Go RS, Broski SM. 18F-FDG PET/CT in Erdheim–Chester Disease: Imaging Findings and Potential BRAF Mutation Biomarker. J Nucl Med 2018;59:774-9.
2. Estrada-Veras JI, O'Brien KJ, Boyd LC, Dave RH, Durham B, Xi L, Malayeri AA, Chen MY, Gardner PJ, Alvarado-Enriquez JR, Shah N, Abdel-Wahab O, Gochuico BR, Raffeld M, Jaffe ES, Gahl WA. The clinical spectrum of Erdheim-Chester disease: an observational cohort study. Blood Adv 2017;1:357-66.
3. Antunes C, Graca B, Donato P. Thoracic, abdominal and musculoskeletal involvement in Erdheim-Chester disease: CT, MR and PET imaging findings. Insights Imaging 2014;5:473-82.
4. Arnaud L, Malek Z, Archambaud F, Kas A, Toledano D, Drier A, Zeitoun D, Cluzel P, Grenier PA, Chiras J, Piette JC, Amoura Z, Haroche J. 18F-fluorodeoxyglucose-positron emission tomography scanning is more useful in follow up than in the initial assessment of patients with Erdheim-Chester disease. Arthritis Rheum 2009;60:3128-38.
5. Catalano OA, Masch WR, Catana C, Mahmood U, Sahani DV, Gee MS, Menezes L, Soricelli A, Salvatore M, Gervais D, Rosen BR. An overview of PET/MR, focused on clinical applications. Abdom Radiol (NY) 2017:42:631-44.
6. Cavaliere C, Romeo V, Aiello M, Mesolella M, Iorio B, Barbuto L, Cantone E, Nicolai E, Covello M. Multiparametric evaluation by simultaneous PET-MRI examination in patients with histologically proven laryngeal cancer. Eur J Radiol 2017;88:47-55.
7. Pan Z, Kleinschmidt-De Masters BK. CNS Erdheim-Chester Disease: A Challenge to Diagnose. J Neuropathol Exp Neurol 2017;76:986-96.
8. Campochiaro C, Tomelleri A, Cavalli G, Berti A, Dagna L. Erdheim-Chester disease. Eur J Intern Med 2015;26:223-9.
9. Haroche J, Charlotte F, Arnaud L, von Deimling A, Hélias-Rodzewicz Z, Hervier B, Cohen-Aubart F, Launay D, Lesot A, Mokhtari K, Canioni D, Galmiche L, Rose C, Schmalzing M, Croockewit S, Kambouchner M, Copin MC, Fraitag S, Sahm F, Brousse N, Amoura Z, Donadieu J, Emile JF. High prevalence of BRAF V600E mutations in Erdheim-Chester disease but not in other non-Langerhans cell histiocytoses. Blood 2012;120:2700-3.
10. Chester W. Ũber lipoidgranulomatose. Virchows Arch A Pathol Anat Histopathol 1930;279:561-602.
11. Blombery P, Wong SQ, Lade S, Prince HM. Erdheim-Chester disease harboring the BRAF V600E mutation. J Clin Oncol 2012;30:e331-2.
12. Martineau P, Pelletier-Galarneau M, Zeng W. The Imaging Findings of Erdheim-Chester Disease: A Multimodality Approach to Diagnosis and Staging. World J Nucl Med 2017;16:71-4.
13. García-Gómez FJ, Acevedo-Báñez I, Martínez-Castillo R, Tirado-Hospital JL, Cuenca-Cuenca JI, Pachón-Garrudo VM, Álvarez-Pérez RM, García-Jiménez R, Rivas-Infante E, García-Morillo JS, Borrego-Dorado I. The role of 18FDG, 18FDOPA PET/CT and 99mTc bone scintigraphy imaging in Erdheim-Chester disease. Eur J Radiol 2015;84:1586-92.
14. Riola-Parada C, García-Cañamaque L, Pérez-Dueñas V, Garcerant-Tafur M, Carreras-Delgado JL. Simultaneous PET/MRI vs. PET/CT in oncology. A systematic review. Revista Espanola de Medicina Nuclear e Imagen Molecular 2016;35:306-12.
15. Goyal G, Heaney ML, Collin M, Cohen-Aubart F, Vaglio A, Durham BH, Hershkovitz-Rokah O, Girschikofsky M, Jacobsen ED, Toyama K, Goodman AM, Hendrie P, Cao XX, Estrada-Veras JI, Shpilberg O, Abdo A, Kurokawa M, Dagna L, McClain KL, Mazor RD, Picarsic J, Janku F, Go RS, Haroche J, Diamond EL. Erdheim-Chester disease: consensus recommendations for evaluation, diagnosis, and treatment in the molecular era. Blood 2020;135:1929-45.
16. Adawi M, Bisharat B, Bowirrat A. Erdheim-Chester disease (ECD): Case report, clinical and basic investigations, and review of literature. Medicine (Baltimore) 2016;95:e5167.
17. Arnaud L, Hervier B, Néel A, Hamidou MA, Kahn JE, Wechsler B, Pérez-Pastor G, Blomberg B, Fuzibet JG, Dubourguet F, Marinho A, Magnette C, Noel V, Pavic M, Casper J, Beucher AB, Costedoat-Chalumeau N, Aaron L, Salvatierra J, Graux C, Cacoub P, Delcey V, Dechant C, Bindi P, Herbaut C, Graziani G, Amoura Z, Haroche J. CNS involvement and treatment with interferon-α are independent prognostic factors in Erdheim-Chester disease: a multicenter survival analysis of 53 patients. Blood 2011;117:2778-82.

18. Aiello M, Cavaliere C, Marchitelli R, d'Albore A, De Vita E, Salvatore M. Hybrid PET/MRI Methodology. Int Rev Neurobiol 2018;141:97-128.
19. Drier A, Haroche J, Savatovsky J, Godenèche G, Dormont D, Chiras J, Amoura Z, Bonneville F. Cerebral, facial, and orbital involvement in Erdheim- Chester disease: CT and MR imaging findings. Radiology 2010;255:586-94.
20. Diamond EL, Dagna L, Hyman DM, Cavalli G, Janku F, Estrada-Veras J, Ferrarini M, Abdel-Wahab O, Heaney ML, Scheel PJ, Feeley NK, Ferrero E, McClain KL, Vaglio A, Colby T, Arnaud L, Haroche J. Consensus guidelines for the diagnosis and clinical management of Erdheim-Chester disease. Blood 2014;124:483-92.
21. Cives M, Simone V, Rizzo FM, Dicuonzo F, Cristallo Lacalamita M, Ingravallo G, Silvestris F, Dammacco F. Erdheim-Chester disease: a systematic review. Crit Rev Oncol Hematol 2015;95:1-11.
22. Loh WJ, Sittampalam K, Tan SC, Chandran M. Symptomatic empty sella syndrome: an unusual manifestation of Erdheim Chester Disease. Endocrinol Diabetes Metab Case Rep 2015;2015:140122.
23. Haroche J, Cluzel P, Toledano D, Montalescot G, Touitou D, Grenier PA, Piette JC, Amoura Z. Images in cardiovascular medicine. Cardiac involvement in Erdheim-Chester disease: magnetic resonance and computed tomographic scan imaging in a monocentric series of 37 patients. Circulation 2009;119:e597-8.
24. Mamlouk MD, Aboian MS, Glastonbury CM. Case 245: Erdheim-Chester Disease. Radiology 2017;284:910-7.

Cite this article as: Garbino N, Punzo B, Todisco A, Cirillo G, Cavaliere C. Whole body positron emission tomography-MRI of Erdheim-Chester disease: a case report. Quant Imaging Med Surg 2020;10(12):2379-2386. doi: 10.21037/qims-19-953

